ChemPubSoc Europe

DOI: 10.1002/chem.201606031

CHEMISTRY A European Journal Full Paper

Single-Ion Magnets

Role of Halide Ions in the Nature of the Magnetic Anisotropy in Tetrahedral Co^{II} Complexes

Shefali Vaidya,[a] Saurabh Kumar Singh,[a, b] Pragya Shukla,[a] Kamaluddin Ansari,[a] Gopalan Rajaraman,*[a] and Maheswaran Shanmugam*[a]

Abstract: A series of mononuclear tetrahedral Co^{II} complexes with a general molecular formula $[CoL_2X_2]$ [L = thiourea and X = Cl (**1**), Br (**2**) and I (**3**)] were synthesized and their structures were characterized by single-crystal X-ray diffraction. Direct-current (dc) magnetic susceptibility [$\chi_M T(T)$ and $M(H)$] and its slow relaxation of magnetization were measured for all three complexes. The experimental dc magnetic data are excellently reproduced by fitting both $\chi_M T(T)$ and $M(H)$ simultaneously with the parameters $D = +10.8\ cm^{-1}$, $g_1 = 2.2$, $g_2 = 2.2$, and $g_3 = 2.4$ for **1**; $D = -18.7\ cm^{-1}$, $g_{iso} = 2.21$ for **2**; and $D = -19.3\ cm^{-1}$, $g_{iso} = 2.3$ for **3**. The replacement of chloride in **1** by bromide or iodide (in **2** and **3**, respectively) was accompanied by a change in both sign and magnitude of the magnetic anisotropy *D*. Field-induced out-of-phase susceptibility signals observed in 10% diluted samples of **1**–**3** imply slow relaxation of magnetization of molecular origin. To better understand the magnetization relaxation dynamics of complexes **1**–**3**, detailed ab initio CASSCF/NEVPT2 calculations were performed. The computed spin Hamiltonian parameters are in good agreement with experimental data. In particular, the calculations unveil the role of halide ions in switching the sign of *D* on moving from Cl^- to I^-. The large spin–orbit coupling constant associated with the heavier halide ion and weaker π donation reduces the ground state–excited state gap, which leads to a larger contribution to negative *D* for complex **3** compared to complex **1**. Further magnetostructural *D* correlations were developed to understand the role of structural distortion in the sign and magnitude of *D* values in this family of complexes.

Introduction

Slow relaxation of magnetization arises in certain oligomeric complexes due to the presence of easy or Ising-type magnetic anisotropy associated with the overall ground state of a molecule. Such compounds are termed single-molecule magnets (SMM), and if the phenomenon originates from a single metal ion or monomeric coordination complex, they are known as single-ion magnets (SIM). Such SMM behavior was first discovered in the $\{Mn_{12}OAc\}$ complex.[1] After this discovery, numerous transition metal complexes[2] flooded the literature with record-breaking ground-state spin ($S = 83/2$ for an Mn_{19} cluster) reported by Powell and co-workers[3] and effective energy barrier for the magnetization relaxation ($U_{eff} = 86$ K for an Mn_6 cluster) by Brechin and co-workers.[4] SMMs can be envisaged for many potential applications such as high-density information storage, spin valves, spintronics, and quantum computing.[5] Over a period of three decades, it has been realized that, due to the random easy-axis orientations in larger clusters, overall magnetic anisotropy *D* becomes small, although complexes were stabilized with relatively large ground-state spin. There are no parameters available to enhance *D* and *S* simultaneously in oligomeric complexes, as is also evident in the fact that the *D* value is approximately equal to $1/S^2$ of the complex.[6] Due to this persistent problem researchers focused their attention on modulating the *D* value of mononuclear transition metal complexes. The majority of the transition metal complexes suffer from small spin–orbit coupling, as the orbital angular momentum is reduced by the ligand field. Restricting the coordination number around the transition metal is a fruitful way to gain orbital angular momentum,[7] and such a synthetic strategy proved successful in two-coordinate Co^{II} and Fe^{I} complexes with the largest anisotropy barriers of 578.2 and 225 K, respectively, reported to date for any transition metal SMMs by Gao and co-workers and Long and co-workers, independently.[8] In addition, several other approaches have been reported in the literature to gain orbital angular momentum and maximize the magnetic anisotropy in mononuclear complexes. For example, using substituents on the ligand to modulate U_{eff} (by means of *D*),[2e,9] in-plane and out-of-plane shifts of the metal ion in five-coordinate Co^{II} complexes,[10] changing the halide ligands in octahedral and certain tetrahedral complexes,[11]

[a] S. Vaidya, Dr. S. K. Singh, P. Shukla, K. Ansari, Prof. G. Rajaraman, Prof. M. Shanmugam
Department of Chemistry, Indian Institute of Technology Bombay
Powai, Mumbai-400076, Maharashtra (India)
E-mail: rajaraman@chem.iitb.ac.in
eswar@chem.iitb.ac.in

[b] Dr. S. K. Singh
Department of Molecular Theory and Spectroscopy
Max-Planck Institute for Chemical Energy Conversion
Mülheim an der Ruhr, 45470 (Germany)

Supporting information and the ORCID identification number for the author of this article can be found under https://doi.org/10.1002/chem.201606031.

structural distortion around metal centers, and even more intricate measures, such as the significant effect of the secondary coordination sphere on modulating the *D* value, which was elegantly explained by Neese and co-workers theoretically and experimentally proven by us recently.[12] To modulate the sign of the magnetic anisotropy, we have recently proposed a synthetic strategy employing a ligand with a soft donor atom (e.g., sulfur) to stabilize easy-axis anisotropy, while a hard donor favors easy-plane orientation of the magnetization.[13]

Along these lines, we intended to probe the influence of other common ligands such as halides in controlling the spin Hamiltonian parameters of the complexes, apart from the soft-donor ligand L. For this purpose, we have synthesized a series of monomeric Co^{II} tetrahedral thiourea complexes and investigated their magnetic properties in detail. The observed change in spin Hamiltonian (SH) parameters and its slow magnetization relaxation behavior of these complexes were rationalized by detailed theoretical calculations.

Results and Discussion

Recently, we and others have pointed out that ligands with soft donor atoms such as sulfur in a tetrahedral Co^{II} environment stabilize easy-axis magnetic anisotropy.[13,14] This proposal has been proven by us recently by employing totally different soft-donor ligands (thiourea and its derivatives).[12c] To probe the influence of the other ligating atoms such as halides beside the soft-donor ligands, we have synthesized a series of monomeric Co^{II} complexes. Treating one equivalent of an alcoholic solution of $CoX_2{\cdot}xH_2O$ (X = Cl, Br, I) with two equivalents of thiourea yielded blue single crystals that were suitable for single-crystal X-ray diffraction. The structure solution and refinement revealed the molecular formula of all three complexes to be $[CoX_2L_2]$ [L = thiourea; X = Cl (**1**), Br (**2**), I (**3**)] (Figure 1). Complexes **1**–**3** crystallized in monoclinic space groups *Cc* (**1**) and $P2_1/c$ (**2** and **3**). The crystallographic parameters for all three complexes are given in Table 1.

In all three complexes the cobalt(II) ion exists in a distorted tetrahedral geometry. Two out of four coordination sites are occupied by the thiourea ligand and the other two by halide ions. The average Co–S distances are 2.302(10), 2.307(9), and 2.319(10) Å for **1**–**3**, respectively. The average Co–X bond length increases with increasing atomic radius of the halide ion (2.258(9) Å for **1**; 2.401(5) Å for **2**; 2.602(5) Å for **3**). The increases in Co–X bond lengths are larger than those of the Co–S bond lengths. The X11-Co1-X12 bond angles in all three complexes are close to the tetrahedral angle: 107.82(3), 108.40(3), and 107.25(2) for **1**–**3** respectively. However, drastic differences are noticed in the S11-Co-S12 bond angles: 96.63(3)° for **1**, 101.43(3)° for **2**, and 100.32°(4) for **3**. Selected bond lengths and bond angles of **1**–**3** are given in Table 2. Detailed structural analysis of all three complexes revealed hydrogen-bonding networks in all directions. In **1**–**3**, the amino protons of the thiourea ligand are involved in hydrogen bonding with halide ions and the sulfur atom. Apart from the intermolecular hydrogen bonding, intramolecular hydrogen bonding also exists in the crystal structure. The atoms involved in both

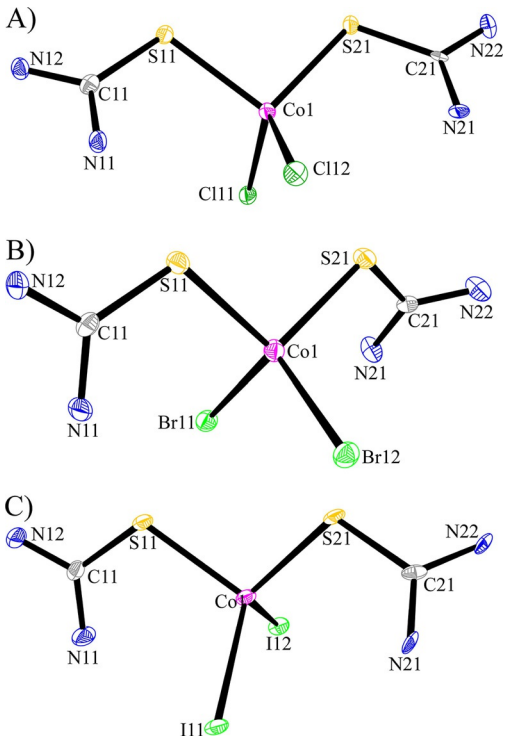

Figure 1. Thermal ellipsoid (50% probability) representation of complexes: A) **1**, B) **2**, and C) **3**.

Table 1. Crystallographic data for complexes **1**–**3**.

	1	2	3
formula	$CoC_2H_8Cl_2N_4S_2$	$CoC_2H_8Br_2N_4S_2$	$CoC_2H_8I_2N_4S_2$
size [mm]	0.20×0.16×0.11	0.35×0.17×0.08	0.58×0.22×0.12
system	monoclinic	monoclinic	monoclinic
space group	*Cc*	$P2_1/c$	$P2_1/c$
a [Å]	8.1970(16)	10.163(4)	10.483(3)
b [Å]	11.528(2)	6.977(2)	7.3377(17)
c [Å]	10.794(2)	14.562(5)	14.813(4)
α [°]	90.0000	90.0000	90.0000
β [°]	103.56(3)	93.207(5)	91.344(3)
γ [°]	90.0000	90.0000	90.0000
V [Å^3]	991.5(3)	1030.9(6)	1139.1(5)
Z	4	4	4
ρ_{calcd} [g cm^{-3}]	1.890	2.390	2.711
$2\theta_{max}$	58.28	58.3	58.34
radiation	Mo K_α	Mo K_α	Mo K_α
λ [Å]	0.71073	0.71073	0.71073
T [K]	100	100	100
reflns	5985	19068	14607
ind. reflns	2585	2770	3046
reflns with $I > 2\sigma(I)$	2310	2065	2251
*R*1	0.0242	0.0304	0.0275
*wR*2	0.0683	0.0478	0.0597

intra- and intermolecular hydrogen bonding are listed in Tables S1–S3 for all three complexes.

The packing diagram of **1** is distinctly different from those of **2** and **3** (Figure 2A). Since complexes **2** and **3** have similar packing arrangements, a representative packing diagram is shown in Figure 2B. In **1**, N–H···S11 (2.624(3) Å) is stronger than N–H···Cl hydrogen bonding (3.093(2) Å). Variation in the

Table 2. Selected bond lengths [Å] and angles [°] for complexes **1**–**3**.

	1	2	3
Co1–S11	2.297(10)	2.303(9)	2.308(10)
Co1–S21	2.307(10)	2.311(9)	2.330(11)
Co1–X11	2.249(9)	2.397(6)	2.595(6)
Co1–X12	2.268(9)	2.405(5)	2.608(5)
X11-Co1-X12	107.82(3)	108.40(3)	107.25(2)
X11-Co1-S11	116.02(4)	111.65(3)	111.86(3)
X12-Co1-S11	106.96(4)	109.87(3)	116.73(3)
X11-Co1-S21	113.46(4)	110.05(3)	110.45(3)
X12-Co1-S21	115.72(4)	115.36(3)	110.07(3)
S11-Co1-S21	96.63(3)	101.43(3)	100.32(4)

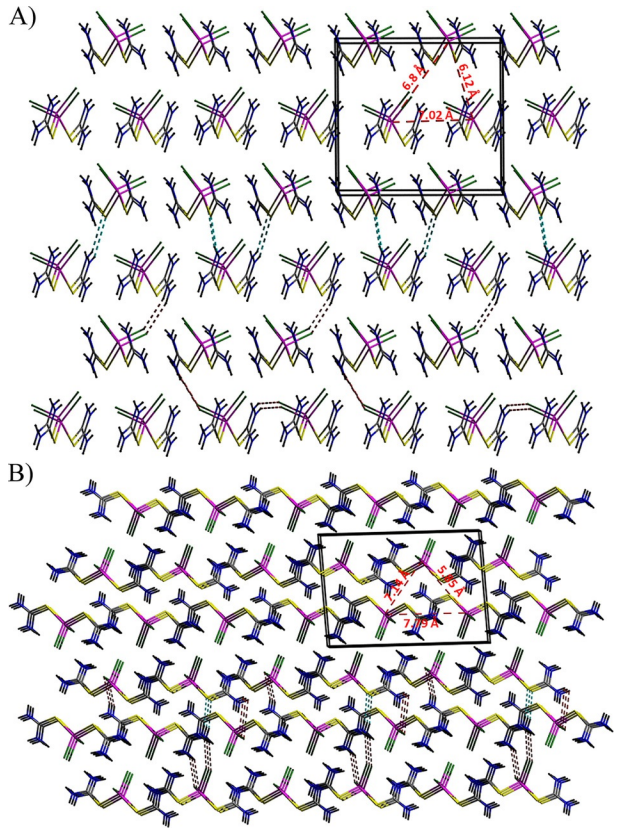

Figure 2. Packing diagrams of: A) **1**, and B) **2**. Sky-blue dotted bonds represent intermolecular hydrogen bonding between sulfur and NH_2 protons, and wine-red dotted bonds denote hydrogen bonding between halide and NH_2 protons in the crystal lattice. Color code: Magenta = Co^{II}, green = X [X = Cl (**1**) or Br (**2**)], blue = N, yellow = S.

hydrogen-bonding strength in **1** is likely due to the short $Co^{II}\cdots Co^{II}$ distance between two molecules (see Figure 2 for details). Such supramolecular interaction is likely to play a significant role in magnetization relaxation dynamics. In the packing diagram of complex **1**, a layer of molecules along the *c* axis are oriented in the same direction, while the adjacent layer is generated by a *c* glide. Although the interatomic $Co^{II}\cdots Co^{II}$ distances in **2** (5.853(3) Å) and **3** (5.932(2) Å) are shorter than that of **1**, the hydrogen-bonding strengths of **2** and **3** are weaker than that of **1** (see Tables S1–S3 and Figure S1 of the Supporting Information for details).

Direct-current (dc) magnetic susceptibility data of 1–3

Variable-temperature dc magnetic susceptibility measurements were performed on polycrystalline samples of all three complexes in the temperature range of 2.0–300 K in the presence of an external magnetic field of 1 kOe (Figure 3). The room-temperature (RT) $\chi_M T$ values for complexes **1**–**3** are 2.40, 2.52, and 2.63 $cm^3\,K\,mol^{-1}$ respectively, which are significantly higher than the expected value for a mononuclear Co^{II} ($S = 3/2$) ion with no first-order orbital angular momentum (1.875 $cm^3\,K\,mol^{-1}$, $g = 2$). The temperature-dependent $\chi_M T(T)$ behavior of all three complexes is almost the same, that is, a gradual decrease in $\chi_M T$ value is found on lowering the temperature from RT to 50 K. The observed temperature dependence in this temperature region (RT to 50 K) for a mononuclear Co^{II} complex indicates depopulation of the Kramers state. The $\chi_M T$ value decreases sharply below 50 K and reaches values of 0.861, 0.900, and 1.240 $cm^3\,K\,mol^{-1}$ at 2.0 K for **1**–**3**, respectively. Several factors, such as magnetic anisotropy associated with the complex, intermolecular antiferromagnetic interaction, and dipolar interactions, are likely to contribute to the sharp decrease in $\chi_M T$ value at low temperature.

Field-dependent magnetization measurements were performed at various temperatures (2–10 K) for **1**–**3** up to 70 kOe. The magnetic moment gradually increases with increasing external magnetic field, and the magnetic moment tends to saturate around 1.95, 2.01, and 2.04 $N\mu_B$ at 2.0 K for **1**–**3** respectively (Figure 3). The fact that the observed magnetic moment at this temperature is significantly lower than the expected value indicates the presence of magnetic anisotropy associated with the ground state in all complexes. The non-superimposable nature of the reduced magnetization curve of all three complexes further supports the presence of magnetic anisotropy (Supporting Information, Figure S2). To extract the spin Hamiltonian (SH) parameters of all the three complexes, we fitted both the $\chi_M T(T)$ and the $M(H)$ data simultaneously using PHI software.[15] The Hamiltonian used for fitting the data is given in Equation (1).

$$H = D\left[S_z^2 - \frac{S(S+1)}{3}\right] + E\left(S_x^2 - S_y^2\right) + g\mu_B HS \qquad (1)$$

To reduce the over parameterization, we fitted the magnetic data with an isotropic *g* value for all complexes except **1**, and the obtained parameters are listed in Table 3. An excellent agreement between the fit and the experimental magnetic data was obtained with the parameters $D = +10.8\ cm^{-1}$ ($g_{xx} = 2.2$, $g_{yy} = 2.2$, $g_{zz} = 2.4$; $|E/D| = 0.11$) for **1**. The simultaneous $\chi_M T(T)$ and $M(H)$ data fit of **2** and **3** yields *D* values of $-18.7\ cm^{-1}$ ($g_{iso} = 2.21$) and $-19.3\ cm^{-1}$ ($g_{iso} = 2.3$) respectively (Table 3). The experimental $\chi_M T(T)$ fit alone is insensitive to the sign of *D*, that is, either with positive *D* or negative *D*, experimental $\chi_M T(T)$ data could be modeled. However, the parameters extracted while incorporating negative *D* for **1** result in un-

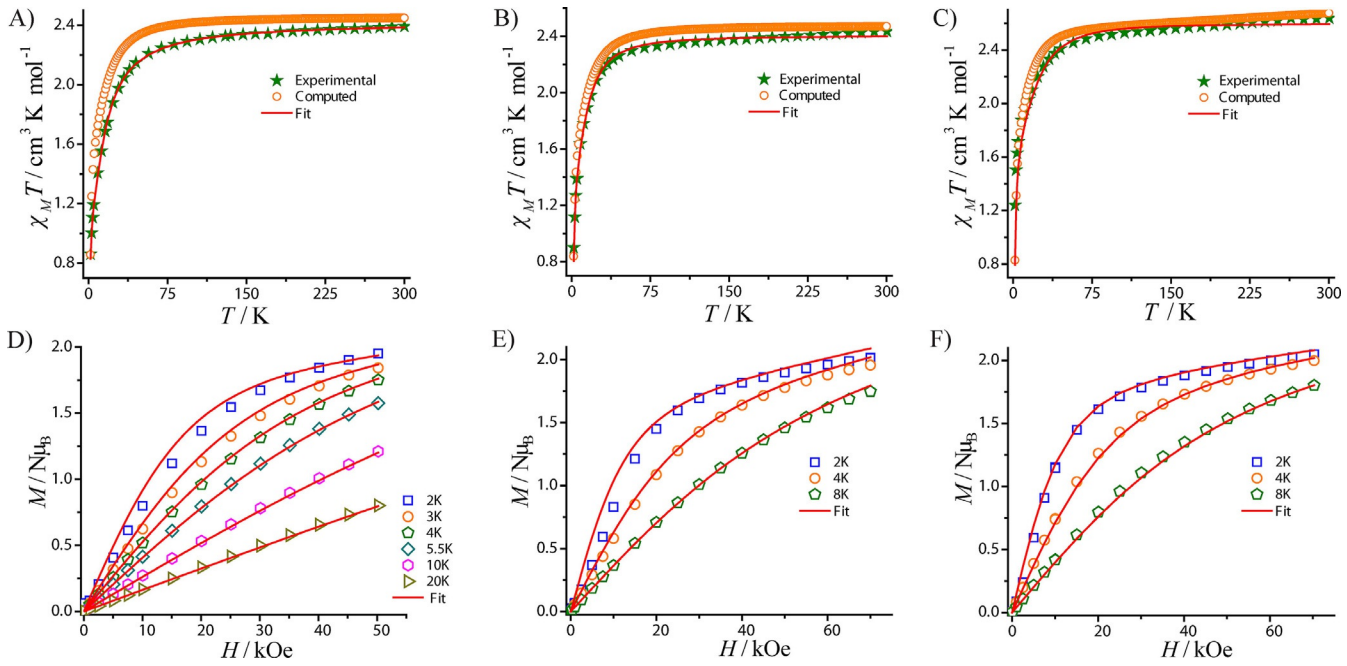

Figure 3. A)–C) Direct-current magnetic susceptibility measurements on polycrystalline samples of **1**–**3** in the presence of an external magnetic field of 1 kOe. The open circles represent the simulation of the experimental magnetic data with the SH parameters computed by CASSCF/ NEVPT2 calculations, as described in the main text. D)–F) Field-dependent magnetization measurements performed at the indicated temperatures. The solid red lines represent the simultaneous fitting of magnetic data [$\chi_M T(T)$ and $M(H)$] with the parameters listed in in Table 3.

Table 3. SH parameters extracted from CASSCF/NEVPT2[a] calculations and PHI[b] fitting[15] for complexes **1**–**3**.

	D_{calcd}[a] [cm^{-1}]	D_{fit}[b] [cm^{-1}]	$\lvert E/D \rvert$ calcd	$\lvert E/D \rvert$ fit	g_{xx}, g_{yy}, g_{zz}[a]	g_{xx}, g_{yy}, g_{zz}[b]
1.	17.4	+10.8	0.25	0.11	2.16, 2.30, 2.41	2.2, 2.2, 2.4
2.	±14.9	−18.7	0.32	–	2.18, 2.29, 2.42	2.21 (g_{iso})
3.	−18.3	−19.3	0.25	–	2.19, 2.29, 2.46	2.3 (g_{iso})

reliable SH parameters (data not shown), while positive D for **2** and **3** yielded poor fits of the $M(H)$ data for these complexes (see Table S4 and Figure S3 of the Supporting Information). This evidently suggests that simultaneous fits of $\chi_M T(T)$ and $M(H)$ magnetic data facilitate reliably extracting the sign and magnitude of the D value for all of the complexes (Table 3). Such an approach is fruitful for unambiguous determination of the sign of D by using dc magnetic data for the majority of the complexes reported in the literature.[13a,16]

The observation of positive D value for **1** is quite different from our earlier prediction,[13a] and we also note that there is a drastic change in magnitude of the magnetic anisotropy in all the complexes compared to the series of $[CoS_4]^{2-}$ complexes reported by us recently.[12c] The notable changes observed in the SH parameters of **1**–**3** are rationalized by detailed theoretical calculations (see below).

EPR measurements on complexes 1–3

To support the parameters extracted from the magnetic data fit, we recorded X-band EPR spectra of **1**–**3** at 5 K for both solids (100% and diluted samples) and frozen solutions. Complex **1** was EPR-silent above 100 K in both solid-state and frozen-solution spectra, while complexes **2** and **3** show broad EPR signals at 100 K (see Figures S4–S6 in the Supporting Information). This is probably due to the intricate electronic structure associated with ^{59}Co(II) ion having a hyperfine spin of $I=7/2$ and its associated fast relaxation phenomenon. Further, accurate determination of zero-field splitting (zfs) by low-frequency EPR spectroscopy is extremely difficult, as its microwave quantum is considerably smaller than the zfs observed in complexes **1**–**3**. At 5.0 K, EPR spectral features of a 100% polycrystalline sample of **1** are distinctly different from those of **2** and **3**, and this suggests that the electronic structure associated with these complexes must be different, whereas **2** and **3** show similar EPR spectral features (see Figure 4). A high-spin Co^{II} complex stabilized with easy-axis anisotropy is expected to be EPR-silent at 5.0 K under strictly axial conditions due to the forbidden $\Delta M_s = \pm 3$ intra-Kramers transition.[11h,17] However, for **2** and **3**, broad EPR transitions arising from the ground Kramers doublets (KDs) observed around 3500 and 9000 G are due to nonzero rhombicity ($E/D=0.32$ for **2** and 0.25 for **3**) associated with these complexes, which mixes the pure wave functions of two KDs. Similar EPR spectral features (broad EPR signals around 3500 and 9000 G) were observed in frozen solutions and magnetically diluted samples of **2** and **3** (see Figures S5 and S6 of the Supporting Information). Such a scenario has been witnessed in many high-spin Co^{II} complexes stabilized with easy-axis anisotropy.[11h,17]

In contrast to complexes **2** and **3**, both frozen solution and 2% diluted sample of **1** show well-resolved peaks indicative of the signal arising from the ±1/2 ground Kramers state ($\Delta M_s =$

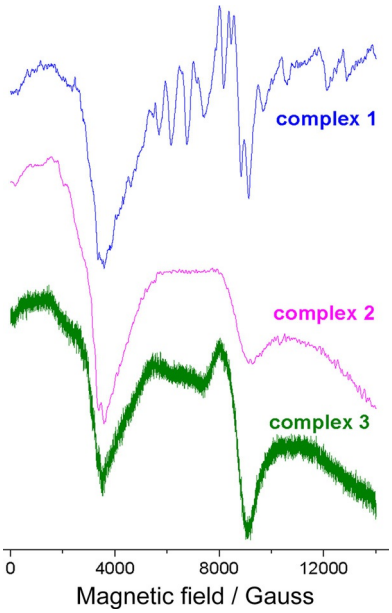

Figure 4. X-band EPR spectra of frozen ethanol/toluene solutions of complexes **1**–**3** recorded at 5 K. Conditions: microwave power = 10(1), 18(2), 20(3) dB [20 mW (**1**), 3.17 mW (**2**), 2 mW (**3**)], modulation amplitude = 0.4 (**1**), 1.45 (**2**), 0.4 mT (**3**), microwave frequency = 9.37 GHz, T = 5 K.

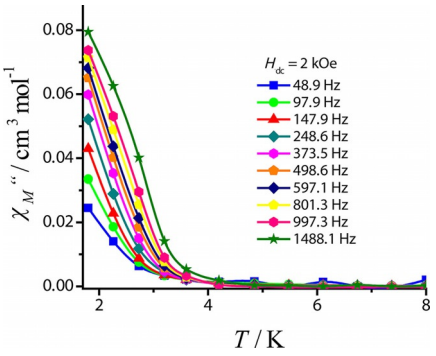

Figure 5. Frequency-dependent out-of-phase susceptibility (χ''_M) signal observed for a 100% sample of complex **1** in the presence of an external magnetic field of 2 KOe at the indicated frequency.

±1; see Figure S4 of the Supporting Information). Variable-temperature EPR spectra recorded on frozen solution evidently show that the intensity of the all the signals decreases with increasing temperature. As low-frequency EPR cannot capture all the EPR spectral features of complex **1**, we have not attempted to simulate the EPR spectrum.

Although the performed EPR experiments do not reveal the magnitude of D accurately, they give strong experimental evidence for the sign of the magnetic anisotropy extracted from the magnetic data fit of complexes **1**–**3**, that is, complex **1** is stabilized with easy-plane anisotropy while **2** and **3** have easy-axis anisotropy. This is further strongly corroborated by ab initio calculations (vide infra).

Alternating-current (ac) magnetic susceptibility data of complexes 1–3

To probe the magnetization relaxation dynamics of all three complexes, ac susceptibility measurements were performed on polycrystalline samples of **1**–**3** with 3.5 Oe ac oscillating field with and without external bias field between 1.8 and 8.0 K. For complex **1**, no frequency-dependent out-of-phase susceptibility signals χ''_M were observed in zero applied field. This is not surprising for a complex (**1**) that has easy-plane magnetic anisotropy. However, when ac data were collected in the presence of a 2 kOe dc bias field, we observed χ''_M signals indicative of field-induced slow relaxation of magnetization (Figure 5).

Similar behavior has been observed for the majority of tetrahedral complexes stabilized with positive anisotropy in the literature.[18] Ruiz and co-workers elegantly explain the slow relaxation of magnetization in a molecule with positive D value.[19] Although complex **1** shows χ''_M signals, the maxima are observed well below the instrumental limit, which hampers extracting the barrier for magnetization relaxation. Surprisingly, although complexes **2** and **3** have negative anisotropy, no frequency-dependent out-of-phase susceptibility signals are observed in ac measurements, both in the presence and absence of an external magnetic field. The absence of χ''_M signals even in the presence of a dc bias field suggests that quantum tunneling of magnetization is much faster compared to the thermal relaxation mechanism (Orbach process). Further, the magnetization relaxation can be triggered by the nuclear hyperfine interaction of Co^{II} and the coordinated halide ions, in addition to the supramolecular interaction mediated through the hydrogen bonding.

In **1**–**3** both intra- and intermolecular hydrogen bonding spread in all directions. Often, such supramolecular interactions lead to faster magnetization relaxation, or the observed slow relaxation phenomenon could be due to magnetic ordering. To understand the role of dipolar interaction and to identify whether the slow relaxation of magnetization is of single-molecular origin or not, we performed ac relaxation dynamics studies on magnetically diluted samples of all complexes (see Experimental Section for details). For all the diluted samples, we observed frequency-dependent out-of-phase susceptibility signals in the presence of an optimum external magnetic field, and this suggests that the slow relaxation of magnetization in **1**–**3** is of single-molecule origin rather a magnetic ordering phenomenon.

To gain more insight into the magnetization relaxation phenomenon, the ac data of all complexes were analyzed in detail. The frequency-dependent out-of-phase susceptibility data of diluted complex **1** are shown in Figure 6, recorded at an optimum field of 5.5 kOe (see Figure S7 of the Supporting Information).

From Figure 6A (also see Figure S8A of the Supporting Information) it is evident that there are two kinds of relaxation, that is, the majority fraction undergoes faster relaxation and a non-negligible fraction exhibits a slow relaxation process. The fast relaxation (major relaxation) and slow relaxation phenomenon observed in **1** are well witnessed in the Cole–Cole plot of the complex, particularly at lower temperature (see Figure 6B). The

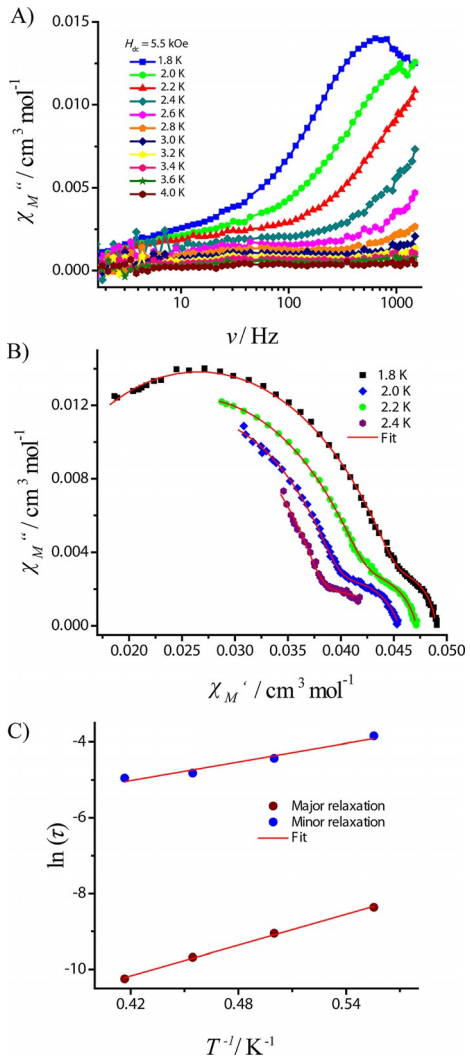

Figure 6. The ac measurements for 10% diluted sample of complex **1**. A) Frequency-dependent out-of-phase susceptibility signals at the indicated optimum dc magnetic field. B) Cole–Cole plots at the indicated temperatures. C) Arrhenius plot of complex **1**. The solid red line represents the fit of the data.

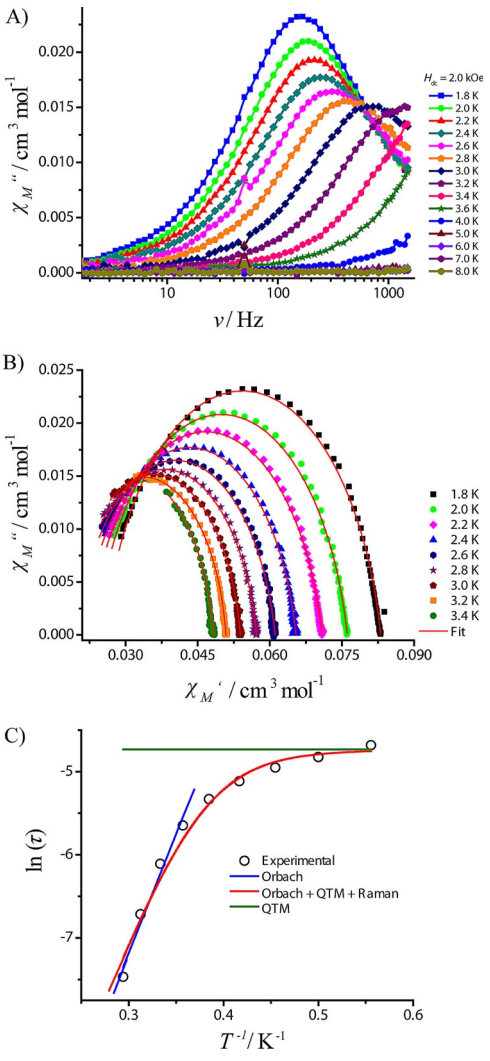

Figure 7. The ac measurements for 10% diluted sample of complex **2**. A) Frequency dependent out-of-phase susceptibility signals at the indicated optimum dc magnetic field. B) Cole–Cole plots at the indicated temperatures. C) Arrhenius plot of complex **2**. The solid red line represents the fit of the data.

Cole–Cole plot of **1** was fitted by considering two relaxation processes in the generalized Debye model [Eq. (2)].

$$\chi_{AC}(\omega) = \chi_{S,tot} + \frac{\Delta\chi_1}{1+(i\omega\tau_1)^{(1-\alpha_1)}} + \frac{\Delta\chi_2}{1+(i\omega\tau_2)^{(1-\alpha_2)}} \cdots \quad (2)$$

The α_1 value ranges from 0.21 to 0.06 and α_2 from 0.07 to 0.6 between 1.8 and 2.4 K (see Table S5 of the Supporting Information). The relaxation times τ_1 and τ_2 extracted from Cole–Cole fitting were employed to construct the Arrhenius plot (Figure 6C). The linear fit of these data considering only the Orbach process results in effective energy barriers of 13.5 K ($\tau_0 = 1.37\times10^{-7}$ s) and 8.15 K ($\tau_0 = 2.2\times10^{-4}$ s).

Contrary to **1** (diluted sample), complex **2** (10% diluted sample) indeed shows well-resolved frequency-dependent χ''_M signals in the presence of an optimum external magnetic field of 2 kOe (Figure 7 and Figure S7 of the Supporting Information). The presence of a single major relaxation is firmly corroborated by the Cole–Cole plot of **2** (Figure 7B and Figure S8B of the Supporting Information). The Cole–Cole plot was fitted by considering a single relaxation process and using the generalized Debye equation [Eq. (3)], and the extracted parameters are listed in Table S6 of the Supporting Information.

$$\chi_{AC}(\omega) = \chi_S + \frac{\chi_T - \chi_S}{1+(i\omega\tau)^{(1-\alpha)}} \quad (3)$$

The α values range between 0.09 and 0.15 in the temperature range of 3.6–1.8 K. This suggests the presence of a narrow distribution of relaxation times. Using the τ values obtained from the Cole–Cole fit, we constructed the Arrhenius plot (Figure 7C). Below 3.5 K, apart from the Orbach process, other relaxation processes (e.g., direct, quantum tunneling of magnetization (QTM), and Raman processes) appear to be operative.

The data were fitted according to Equation (4), which takes into account various relaxation processes.

$$\frac{1}{\tau} = \frac{1}{\tau_{QTM}} + AH^2T + CT^n + \frac{1}{\tau_0}\exp\left(\frac{-U_{eff}}{k_BT}\right) \quad (4)$$

where $1/\tau_{QTM}$ represents relaxation by QTM, AH^2T the direct process, CT^n the Raman process, and the last term describes the relaxation by the Orbach process.

It is not necessary to use all the relaxation processes to fit the Arrhenius plot of **2**. By considering only Orbach (28.6 K, $\tau_0 = 1.66\times10^{-7}$ s), QTM (0.0088 s), and Raman ($C = 0.065\ s^{-1}\ K^{-3}$ and $n = 6$) processes, an excellent fit to the experimental data was obtained.

In line with the magnetization relaxation behavior of **2**, complex **3** (10% diluted sample) also exhibits similar relaxation behavior (Figure 8), but a slightly higher dc bias field (H_{dc} = 5.5 kOe, Figure S7 of the Supporting Information) is required to observe the frequency-dependent out-of-phase susceptibility signals of **3** compared to **2** (H_{dc} = 2 kOe). The τ value extracted from Cole–Cole fitting data was employed to construct the Arrhenius plot (see Table S7 of the Supporting Information). The experimental data were fitted by considering multiple relaxations [Eq. (4)]. A reasonably good fit was obtained by taking into account only Orbach (9 K, $\tau_0 = 4.06\times10^{-4}$ s), Raman ($C = 0.034\ s^{-1}\ K^{-3}$, $n = 6$), and QTM (0.007 s) processes (see Figure 8C).

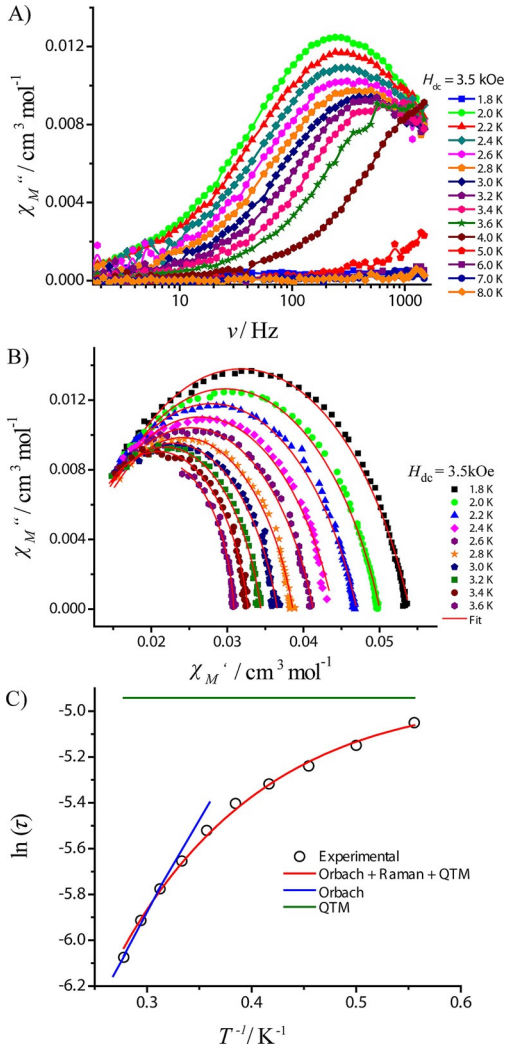

Figure 8. The ac measurements for 10% diluted sample of complex **3**. A) Frequency-dependent dependent out-of-phase susceptibility signals at the indicated optimum dc magnetic field. B) Cole–Cole plots at the indicated temperatures. C) Arrhenius plot of complex **3**. The solid red line represents the fit of the data.

To fully understand the magnetization relaxation dynamics observed in all three complexes, the trends in the estimated magnetic anisotropy, and to unequivocally establish the role of halide ions in modulating the *D* and *E* values, ab initio calculations were performed on complexes **1**–**3**.

Computational studies on complexes 1–3

CASSCF and NEVPT2 calculations were performed on complexes **1**–**3** to understand the origin of positive (**1**) and negative (**2** and **3**) zfs parameters in these complexes (see Experimental Section). We also attempted to shed light on the role of structural distortions in the magnetic anisotropy of these complexes. The computed SH parameters (*D*, *E*, and g values) for all three complexes are listed in Table 3. The simulation of experimental magnetic susceptibility data with the computed SH parameters is in good agreement (Figure 3), which reflects the reliability of the computed parameters. It is evident from Table 3 that ab initio calculated $|E/D|$ values are quite large for all three complexes.

Particularly for complex **2**, the $|E/D|$ value is significantly large and is close to the rhombic limit ($|E/D| \approx 0.3$); therefore, the sign of *D* in complex **2** cannot be predicted unambiguously by calculation. Although single-crystal X-ray diffraction studies reveal that all three complexes have distorted T_d geometry, in reality they have only C_{2v} symmetry. Thus, lowering of symmetry allows rigorous mixing between the ground and the excited states, which leads to a large zfs in these complexes. The tetrahedral Co^{II} ligand field terms are $^4T_2(F)$, $^4T_1(F)$, and $^4T_1(P)$, which further split into ($^4A_2 + {}^4B_1 + {}^4B_2$), ($^4A_1 + {}^4B_1 + {}^4B_2$), and ($^4A_2 + {}^4B_1 + {}^4B_2$) states, respectively, in C_{2v} symmetry, and thus a total of nine spin-allowed transitions is possible. The computed spin-allowed d–d transitions are listed in Tables S8–S11 of the Supporting Information (see also Figure S9). The d–d transitions belonging to the single excitations $^4A_2 \rightarrow {}^4T_2(F)$ and $^4A_2 \rightarrow {}^4T_1(F)$ are found below 10000 cm^{-1} (see Table 4 for details), and this explains why the UV/Vis absorption spectra recorded for all three complexes did not capture these transitions. On the other hand, the transition that arise from the double excitations $^4A_2 \rightarrow {}^4T_1(P)$ are captured in the UV/Vis absorption spectrum. Three distinct peaks are observed for all three complexes (features of low symmetry) in the range of 525–825 nm (see Figure 9) The d–d transitions computed at the CAS (7,5 and 13,8) level of theory (see Computational Methods section for the details of the active space) are overestimated compared to experiment, and this is likely due to the lack of dynamic correlation. However, inclusion of the dynamic correlations by using the NEVPT2 method yields slightly better results. The calculat-

Table 4. CASSCF (7,5)+NEVPT2 computed SH parameters (g, D, $|E/D|$) and state-by-state contributions to the D values [cm^{-1}].

State	1		2		3	
	CASSCF	NEVPT2	CASSCF	NEVPT2	CASSCF	NEVPT2
$^4T_2(F)$	26.46	18.99	27.46	19.03	12.22	7.74
	16.14	10.94	16.64	11.05	12.75	8.09
	−19.52	−13.48	−25.04	−16.67	−59.81	−40.01
	−2.909	−2.949	−2.747	−2.760	−2.289	−2.277
^2G	5.084	5.322	5.409	5.454	4.829	4.853
	1.054	1.089	−1.375	−1.391	−1.848	−1.813
D_{tol}[a]	21.69	17.38	18.84	14.89	−24.68	−18.31
$\|E/D\|$	0.26	0.25	0.33	0.31	0.23	0.25
g_{xx}	2.2172	2.1596	2.2663	2.1878	2.2856	2.1941
g_{yy}	2.4125	2.3001	2.4211	2.2983	2.4238	2.2936
g_{zz}	2.5539	2.4101	2.5774	2.4154	2.6644	2.4675

[a] D_{tol} = The summation of contribution from the entire 10 quartet and 40 doublet states, thus it might vary from the summation of the listed major contributions.

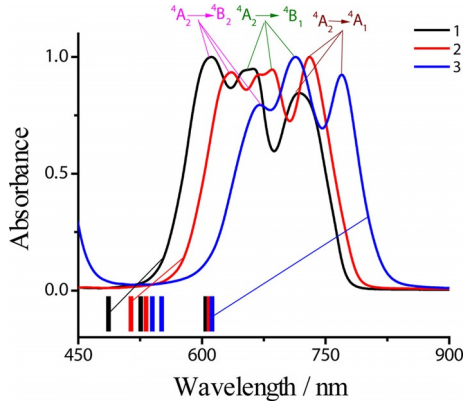

Figure 9. UV/Vis absorption spectra of **1**–**3** in ethyl acetate solution in the range of 450–900 nm. Colored sticks represent the computed absorption bands for $^4A_2 \rightarrow {}^4T_1(P)$ transitions at the CAS(13,8) level of theory.

ed absorption spectra for all complexes **1**–**3** along with experimental observations are provided in the Supporting Information (see Figure S9). Despite the high-level theory employed to reproduce the UV/Vis spectra, apparent deviations from experiments are still noted. This is attributed to the fact that the calculations performed include only selected electrons in the reference space; while this is generally sufficient for magnetic anisotropy, a very large reference space including that of the ligands is required to reproduce the exact positions of the absorption spectra. This has been witnessed earlier in several mononuclear complexes.[12a,20] Both experimental and computed d–d transitions show a redshift on moving from Cl to I in complexes **1**–**3**, and this is essentially due to the fact that the iodide ligand provides smaller crystal-field splitting and low interelectronic repulsion, which result in low-lying excited states. For all complexes **1**–**3**, the ground-state wave function is heavily mixed with other excited states. For **1**, the ground state has 48% of $(d_{x^2-y^2})^2(d_{z^2})^2(d_{xy})^1(d_{xz})^1(d_{yz})^1$ composition and 26% of $(d_{x^2-y^2})^1(d_{z^2})^2(d_{xy})^2(d_{xz})^1(d_{yz})^1$ composition.

The mixing is even more rigorous for the Br and I analogues (see Supporting Information for details). Not only the single-excitations, but also the states arising from the double excitations are found to be strongly mixed with the ground-state wave function. This highlights the need for a genuine multireference method to compute the spectroscopic properties of these systems.[21] To understand the origin of magnetic anisotropy in this class of complexes, we first analyzed the state-by-state contributions and then correlated these transitions with the orbital ordering. The state-by-state contribution to the D value for **1**–**3** is detailed in Table 4. From Table 4, it is evident that the largest contribution to the D value arises from the $^4T_2(F)$ excited state (assuming a T_d environment), while other quartet states marginally contribute to the D value. Among these three transitions, two transitions make positive contributions to the D value, whereas the third transition always contributes to the negative D value.

This is due to the different nature of the transition dipole moments (see below). Apart from the quartet $^4T_2$ state, we also noted some contribution from the low-lying ^2G state; however, it has little effect on the overall zfs parameter. Here, we have provided the splitting pattern of the low-lying excited states for complex **3** (see Figure 10). The observed splitting pattern is in line with previous studies on low-symmetry Co^{II} complexes. We analyzed CAS (7,5) orbitals to rationalize these different contributions to the D value. The energy ordering of the CAS (7,5) orbitals is provided in Figure 11, and is accordance with

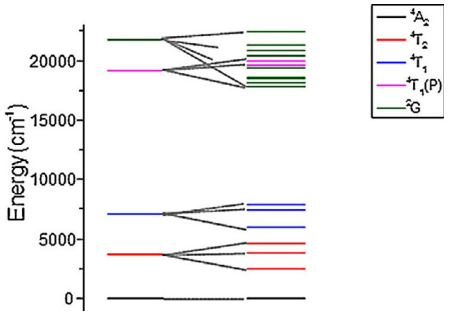

Figure 10. The splitting pattern of the few low-lying quartet and doublet states ($^4T_2(F)$, $^4T_1(F)$, $^4T_1(P)$ and ^2G) for complex **3**.

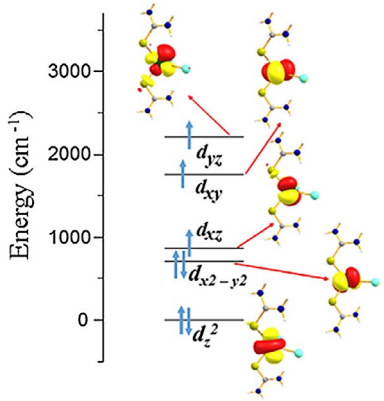

Figure 11. A) CASSCF computed energies of metal-based d-orbitals of complex **3**. B) Color code: Co (green); S (light yellow); I (turquoise); N (blue); C(gray); H (white).

ligand-field paradigm for C_{2v} symmetry. The three different excitations corresponding to $^4T_2$ can be assigned as excitation from the $(d_{x^2-y^2})^2 \rightarrow t_2$ subshell $[(d_{xy})^1(d_{xz})^1(d_{yz})^1]$. The negative contribution to the *D* value is due to spin-conserved excitation of $(d_{x^2-y^2})^2 \rightarrow (d_{xy})^1$ orbitals, as both orbital belong to the same $|m_l|$ level. The other two excitations $(d_{x^2-y^2})^2 \rightarrow (d_{yz})^1/(d_{xz})^1$ lead to a positive zfs contribution (see Table 4 for details).[19]

The small contributions from the low-lying doublet $^2T_2$ (^2G) states are due to the intra-SOMO transitions within the t_2 subshell. Inclusion of the dynamic correlations slightly decreases the magnitude of the *D* value, but its sign remains unchanged. This is due to the fact that the dynamic correlation strongly stabilizes the ground state compared to the excited quartet state, and this led to an increase in the energy gap between the ground and excited quartet state, which eventually decreases the magnitude of the *D* value. On the other hand, doublet states are strongly affected by the dynamic correlation, but transitions of similar magnitude and opposite sign cancel each other out, and this leads to a negligible contribution to the total *D* value. The orientation of the *D* tensor for complexes **1**–**3** is shown in Figure 12.

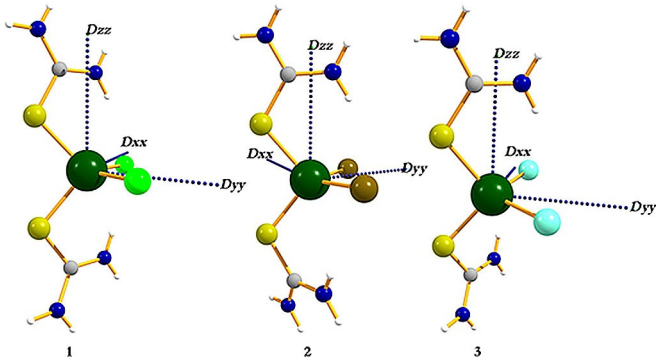

Figure 12. NEVPT2 calculated orientation of the main magnetic axes (*D* tensor) for: A) 1, B) **2**, and C) **3**. Color code Co (green); S (yellow); Cl (light green); Br (brown); I (turquoise); N (blue); C (gray); H (white).

The negative contribution to the *D* value increases on moving from Cl to I, and this may be due to the fact that the large spin–orbit coupling constant associated with the heavier halide brings the excited states closer to the ground state, and hence the magnitude of the *D* value increases (see Table 4 for details).[22] To cross-check whether it is an effect of heavier halide or local structural distortion (S-Co-S 96(1) and 100(3)°), we performed additional calculations on a model complex of **3** in which the I ligand is substituted by Cl, without altering the Co–Cl bond length (**3a**). Calculations on model complex **3a** yielded a *D* value of $+17.4\ cm^{-1}$ and $|E/D|$ value of 0.19, very similar to those of complex **1** (see Figures S10 and S11 in the Supporting Information). This clearly highlights that the zfs of the Co^{II} ion in complexes **1**–**3** is influenced more strongly by the presence of a heavier ligand such as iodide in the first coordination sphere than by the local structural distortions.

This is in line with previous observations on pseudo-tetrahedral Co^{II} complexes, for which the sign of the *D* value was found to be sensitive to the nature of the metal–ligand interaction (negative *D* for soft ligands).[12–14] The rhombic zero-field splitting *E* arises due to the difference between the D_{XX} and D_{YY} components; the larger the difference, the larger the *E* value. The difference in the D_{XX} and D_{YY} components can be traced back to the different strengths of the single-electron excitation from the e subshell to d_{xz} and d_{yz} orbitals of the t_2 subshell. We have observed a significant splitting between the d_{xz} and d_{yz} orbitals, and this eventually led to a large difference between the D_{XX} and D_{YY} components; hence, the large $|E/D|$ values. The large splitting between the d_{xz} and d_{yz} orbitals is due to the presence of two different donor atoms having different σ/π-donor abilities. The d_{xz} orbital interacts with a sulfur atom, and the d_{yz} orbital interacts with an X^- ion, and this leads to a large splitting between these two orbitals in all three complexes. On the other hand, the presence of four sulfur atoms would result in nearly degenerate d_{xz}/d_{yz} orbitals and thus lower $|E/D|$ values, as observed earlier by us for $[CoS_4]^{2+}$ SMMs.[12c]

To understand the impact of metal–ligand covalency on the zfs parameter, it is of prime importance to extend the active space by incorporating some ligand orbitals that strongly mix with metal-based orbitals, that is, ligand orbitals with sizable tails on the metal center. For the tetrahedral Co^{II} complexes here, we considered the three σ-bonding orbitals ($d_{xz}+L$, $d_{yz}+L$ and $d_{xy}+L$, where L = ligand orbitals) in the active space to describe the metal–ligand covalency. Incorporation of these three σ-bonding orbitals offers a way to analyze the effect of ligand-to-metal charge transfer on magnetic anisotropy. One can also incorporate the π orbitals in the active space, but σ bonds offer a better picture of metal–ligand covalency, as σ overlaps are more pronounced than π overlaps. With an extended active space of CAS(13,8), we computed all ten quartets and forty doublets in the configuration interaction module for all the three complexes. The computed *D* ($|E/D|$) values are $+19.2$ (0.27) for 1, ± 16.9(0.33) for **2** and -22.4 (0.21) for complex **3** The computed $|E/D|$ values are in line with previous calculations with minimal active space of CAS(7,5), that is, seven Co^{II}-based electrons in five Co^{II}-based orbitals. However, the computed *D* values with CAS(13,8) are marginally ($\approx$2–4 cm^{-1}) higher than that computed with the minimal active space of CAS(7,5). Interestingly, the increment in the *D* value is found to be largest for **3** and smallest for **1**. To correlate these changes in the *D* values with the metal–ligand covalency, we analyzed the eigenvalue plots of complexes **1**–**3**. Figure 13 shows two important features: 1) splitting of the d manifold lies in a narrow region on moving toward the heavier halides and 2) the σ-bonding orbitals are much closer in energy to the metal-based d orbitals for complex **3** than for **2** and **1** (Figure 13).

The first feature is essentially due to the weak ligand field offered by the heavier halido ligands, which results in a smaller crystal-field splitting. The second feature highlights the increase in the metal–ligand covalency, whereby the gap between the metal- and ligand-based orbitals decreases on moving to the heavier halide. The decrease in the gap between these orbitals leads to strong overlap, which is directly

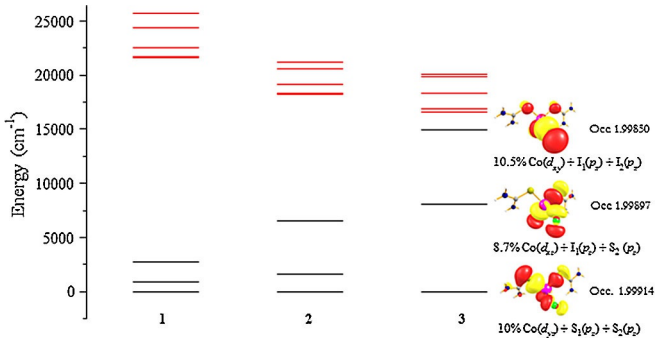

Figure 13. CASSCF computed orbital energies for complex **1**–**3**. The thick black lines represent the σ-bonding orbital, and the red lines the d-orbital splitting.

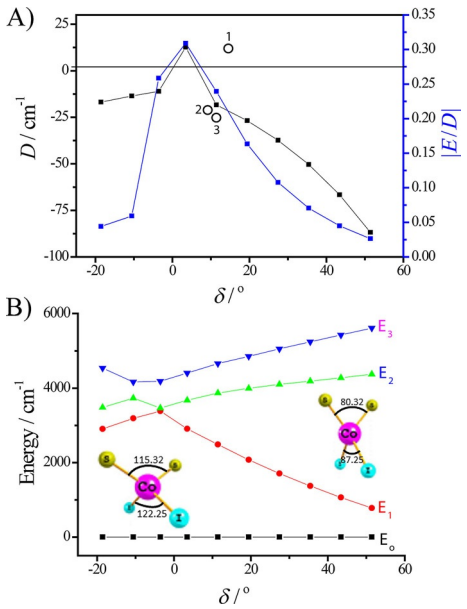

Figure 14. A) Variation of the D and $|E/D|$ values with changing δ value along with the corresponding parameters observed for complexes **1**–**3**. The D value observed for complexes **1**–**3** is mapped (open circle symbol) in the correlation developed on basis of the δ value of the respective complexes. B) Energy variation of the ground and first three excited states originating from ^{4}T with respect to the change in the δ value. The graphs constructed here are based on the values computed at the NEVPT2 level of theory. The experimentally obtained SH parameters of complexes **1**–**3** are mapped on the developed magneto-structural correlation.

proportional to the degree of covalency (see the coefficients in Figure 13).[23] Thus, the near degeneracy between the ligand- and metal-based orbitals explains the important contribution of the ligand-to-metal charge-transfer excitations in the ground-state wave function. Not only the D value, but also the absorption spectrum have significantly improved by extending the active space (see Table S11 in the Supporting Information). Furthermore, incorporation of a double shell that increases the radial electron correlation may further improve the obtained spectroscopic properties.[24] Finally, our study suggests that the extended active space calculations offer a clear picture of metal–ligand covalency and its effect on the magnetic anisotropy. Our calculations demonstrate that the presence of large spin–orbit coupling associated with heavier halides is not the sole factor increasing the zfs of transition metal complexes, as metal–ligand covalency drastically affects the nature of excitations and thus the zfs.[25]

Magnetostructural *D* correlation

To further understand the influence of structural parameters on the sign and magnitude of the D value in tetrahedral Co^{II} complexes, we developed a magnetostructural correlation for **3**. We systematically varied the S-Co-S and I-Co-I bond angles to generate tetragonally compressed and elongated structures.[24] In complex **3**, the S-Co-S and I-Co-I bond angles are 100 and 107° respectively, which suggests that **3** has an elongated tetrahedral geometry. We defined a δ parameter [$\delta = 2T_d - (\alpha + \beta)$, where T_d is the tetrahedral angle of 109.5°, α the S-Co-S bond angle, and β the I-Co-I bond angle] and developed a correlation based on the variation in the δ value. A negative value of δ represents flattening of the tetrahedral geometry, while a positive value represents a tetragonally elongated geometry (see Figure 14 for details). With increasing δ value, the D value increases linearly, and for the largest δ value of 50°, the D value was as high as $-86\ cm^{-1}$. Thus, we observed a fourfold increase in the D value compared to parent complex **3** ($\delta = 11.4$).

Besides, the $|E/D|$ value also decreases with increasing δ. We plotted the variation of the D and $|E/D|$ values with δ value along with variation of the first three excited state E_1, E_2, and E_3, which belong to $^4T_2(F)$ in T_d symmetry, and the ground state with the δ value. The gradual increase in the D value with increasing δ value is due to the lowering of the first excited state (E_1) close to the ground state. However, the other two excited states E_2 and E_3 show an antagonizing behavior, moving away from the ground state, as the δ value increases. The splitting pattern of the first three excited states for the structures corresponding to the large δ values show a typical splitting pattern associated with D_{2d} symmetry, whereby the $^4A_2$ ground state transforms into a $^4B_2$ state and the first excited state $^4T_2$ splits into $^4B_1$ and ^4E states.

The close proximity of the $^4B_1$ state to the $^4B_2$ ground state is the key to the giant zfs associated with Co^{II} complexes in D_{2d} point group.[12,26] On the other hand, the nondegenerate nature of second and third excited states (^4E for D_{2d} symmetry) is due to the asymmetry in the bond angle and difference in the donor strength of ligands. In the other half of the magnetostructural correlations, decreasing δ value slowly decreases the D value at a δ value of +3.45 (close to tetrahedral), but we did not notice a change in the sign of the D value.

The sign of D cannot be determined unambiguously for this structure, as $|E/D|$ reaches as high as 0.3 at this δ value (+3.45). The decrease in the magnitude of the D value can be directly correlated with energy of the first excited state, which is higher for complexes with small δ values. Unlike the scenario observed for tetragonal elongation, the D value does not change abruptly in tetragonally compressed Co^{II} geometry. The developed correlations highlight the importance of tetragonal

compression and elongation, which are directly correlated with the sign and magnitude of the *D* value of $\{CoL_2X_2\}$-type complexes.

Finally, to shed light on the SMM characteristics of these complexes, we first analyzed the wave function of the ground-state KD. In all three complexes, the ground-state KD is not well isolated, and is strongly mixed with other, excited-state KDs. For complex **3**, the ground state KD (represented as $|S,\pm M_s\rangle$) is composed of 80% $|3/2,\pm 3/2\rangle$ and 18% $|3/2,\pm 1/2\rangle$ components, which is in principle forbidden for a Kramers ion. For the Kramers ion, these two states must be orthogonal in zero field, and therefore QTM effects are expected to be absent. However, the large *E* term allows mixing between the ground and excited KDs. This mixing of the state and the apparent splitting of these states by the large hyperfine spin of Co^{II} triggers QTM, even in zero field. This could be one of the possible reasons behind the absence of zero-field SMM characteristic in complex **3**. This has been witnessed earlier in other mononuclear Co^{II} complexes (see Table S12 in the Supporting Information).[19] Interestingly, for complex **1**, we observed an out-of-phase signal in the presence of applied magnetic field.[18,27] To understand this scenario, we first analyzed decomposition of the ground-state wave function, and for complex **1** the ground-state KD is composed of 70% $|3/2,\pm 1/2\rangle$ and 22% $|3/2,\pm 3/2\rangle$. Such strong mixing between the ground and excited KDs occurs due to the presence of a large *E*/*D* term ($E/D\approx 0.24$). In principle, for $M_s = 1/2$, there is no preferred easy axis for magnetization in the presence of purely axial symmetry. However, the presence of a large *E* term $[(D_{xx}-D_{yy})/2]$ creates a preferred easy axis of orientation in the *xy* plane. The relaxation is enabled in the $-x(-y)$ to $+x(+y)$ direction depending on the sign of the *E* term. However, for $M_s = 1/2$ as the ground state, the strong QTM leads to faster relaxation. On the other hand, if one applies a static dc field, the QTM is suppressed and a slow relaxation can be observed. In the literature, there are several examples in which Co^{II} complexes show field-induced SMM characteristics, even with positive zfs.[19] In such cases, the barrier height can be assigned as $2|E|$ $(D_{xx}-D_{yy})$ rather than $2|D|$. The computed energy barrier for complex **1** is approximately $2|E| = 6.09$ K, which is good agreement with U_{eff} of complex **1** ($U_{eff} = 13.5$ and 8.15 K for major and minor relaxation, respectively). The presence of field-induced SIM behavior in complex **1** is due to the presence of positive zfs with remarkably large $|E/D|$ value. Interestingly, the large $|E/D|$ terms offers a key for molecules to show slow relaxation of magnetization with positive *D* values.

Conclusions

We have isolated a series of tetrahedral Co^{II} complexes with the general molecular formula $[CoL_2X_2]$ [X = Cl (**1**), Br (**2**), I (**3**)], which were structurally characterized by single-crystal X-ray diffraction. Direct-current magnetic susceptibility measurements performed on polycrystalline samples of all complexes indicate the presence of magnetic anisotropy. The parameters extracted from magnetic data fitting [simultaneous fitting of $\chi_M T(T)$ and $M(H)$] of all the complexes are in excellent agreement with the experimental magnetic data, and suggest reliability of the extracted parameters. The magnetic data fitting evidently shows that complex **1** stabilizes easy-plane magnetic anisotropy, while **2** and **3** have easy-axis magnetic anisotropy. This is qualitatively supported by EPR measurements on these complexes. Alternating-current magnetic susceptibly measurements were performed on all complexes, but none of them shows frequency-dependent out-of-phase susceptibility χ''_M in the absence of an external magnetic field. On the other hand, ac measurements on 10% diluted samples of **1**–**3** apparently showing χ''_M signals in the presence of an optimum external magnetic field suggest that the slow relaxation phenomenon originates from single molecules, which also signifies the influence of dipolar interaction on magnetization relaxation dynamics. The nature of the extracted SH parameters and observed magnetization relaxation behavior was rationalized by electronic-structure calculations. Calculations suggest that the large negative *D* value for complex **3** compared to **1** and **2** is due to the higher metal–ligand covalency of the Co–I bond compared to the Co–Cl and Co–Br bonds in **1** and **2** respectively. The increase in the metal–ligand covalency has a positive impact on stabilizing easy axes of anisotropy in Co^{II} complexes. Also, we rationalize that the absence of slow magnetic relaxation behavior in **1**–**3** is due to the lack of a pure ground state in all complexes, and further the large $|E/D|$ value effectively triggers QTM rather than a thermally assisted Orbach process.[2l,28] The lack of an isolated ground state and the large $|E/D|$ value are correlated and were traced back to the structural distortion present in all complexes. In addition, the hyperfine interaction is likely to make a non-negligible contribution to the QTM behavior observed in all complexes. Overall, the present study reveals that not only soft donors such as sulfur modulate the sign and magnitude of *D* (which is the case in some of the recent reports), but also other ligands such as halides holds the key to altering the magnitude and sign of the *D* value of complexes. Further, the study reveals that heavier ligating atoms with large spin–orbit coupling enhance the metal–ligand covalency, which tends to stabilize easy-axis magnetic anisotropy in tetrahedral Co^{II} complexes. To generalize further, surrounding a tetrahedral Co^{II} ion by soft-donor ligands of similar π/σ strength ought to stabilize easy-axis anisotropy with small $|E/D|$ ratio. This is an useful finding, particularly for synthetic chemists involved in discovering a new generation of SIMs.

Experimental Section

All chemicals were purchased from commercial sources (Alfa Aesar and Sigma-Aldrich). All reactions were performed under aerobic conditions. A PerkinElmer FTIR spectrometer (400–4000 cm^{-1}) was used to collect the IR spectra for polycrystalline samples by using KBr pellets. Magnetic susceptibility measurements were performed with an MPMS-XL SQUID magnetometer equipped with 7 T magnet in the range 300–2.0 K. The single-crystal X-ray data were collected with a Rigaku-Saturn CCD diffractometer. Details of data collection and structure solution methods were reported elsewhere.[12c] Elemental analysis was carried out with a Thermo Finnigan device. The powder XRD data were collected with a Panalytical

MRD System. The absorption profile for all the complexes were recorded with a Jasco V-530 UV/Vis spectrophotometer. EPR spectra were recorded on a Bruker EMX-plus X-band spectrometer (9.37 GHz).

Computational methods

All quantum chemical calculations were performed on the X-ray structures with ORCA[21b,29] code. To compute the nature of low-lying excited states and zero-field splitting parameters, we used multireference ab initio calculations. CASSCF calculations with *N*-electron valence perturbation theory (NEVPT2) were performed on complexes **1**–**3**. NEVPT2 calculations were performed on top of the converged CASSCF wave function to recover the dynamic correlation.[30] Scalar relativistic effects were treated by using a second-order Douglas–Kroll–Hess (DKH) method.[31] All these procedures were carried out with all electron segmented def2-TZVP basis set for all atoms. The resolution of identity (RI) approximation was used with the corresponding auxiliary basis sets to speed up the calculations.[32] Two sets of calculations were performed with two different active spaces. The first active space was the minimal active space comprising seven active d electrons in the five Co^{II}-based d orbitals [CAS(7,5)]. Herewith, we computed all ten quartet and 40 doublet states. To understand the effect of the ligands, especially the nature of metal–ligand covalency, we extended the active space by incorporating three σ-bonding orbitals. Hence, the new active space is CAS(13,8): six electrons of the 3 σ-bonding orbitals and seven d electrons in the five active Co^{II}-based d-orbitals. The ten quartets and 40 doublets were computed with CAS(13,8) active space. Apart from computing the SH parameters, we also performed surveys for fitting of magnetization and susceptibility data to check the quality of fit.

Synthesis of $[Co(L)_2Cl_2]$ (1)

Solid $CoCl_2{\cdot}6H_2O$ (1.55 g, 6.5 mmol) was added to ethanol at 35–40 °C. Ligand L (1 g, 13.2 mmol) was added and the reaction mixture was heated under reflux for 12 h. The solvent was removed under reduced pressure (rotovap) after cooling the reaction mixture. The complex of interest was extracted with acetonitrile. Needle-shaped, blue single crystals were grown by diffusion of diethyl ether into the acetonitrile solution for one week at room temperature. Yield: 1.2 g (32.4%). Elemental analysis calcd (%): C 8.5, H 2.8, N 19.8, S 22.7; found: C 8.42, H 2.3, N 19.6, S 22.1; IR (KBr): $\tilde{\nu}$3329, 3391 (ν_{NH_2}), 1620 cm^{-1} ($\nu_{C=S}$).

Synthesis of $[Co(L)_2Br_2]$ (2)

A similar synthetic procedure was followed as for **1**, but $CoBr_2$ (1.43 g, 0.0065 mol) was used in place of $CoCl_2{\cdot}6H_2O$, and the product was extracted with ethyl acetate rather than acetonitrile. Single crystals were obtained by slow evaporation of the ethyl acetate solution. X-ray-quality blue single crystals grew from the filtrate over a week at room temperature. Yield: 1.7 g (35.4%). Elemental analysis calcd (%): C 6.5, H 2.17, N 15.1, S 17.3; found: C 6.38, H 2.5, N 14.84, S 17.5; IR (KBr): $\tilde{\nu}$ = 3313, 3391 (ν_{NH_2}), 1634 cm^{-1} ($\nu_{C=S}$).

Synthesis of $[Co(L)_2I_2]$ (3)

A similar synthetic procedure was followed as for **2**, except that CoI_2 (2.05 g, 0.0065 mol) was used in place of $CoBr_2$. Yield: 0.7 g (11.4%). Elemental analysis calcd (%): C 5.2, H 1.7, N 12.1, S 13.8; found: C 5.16, H 2.1, N 11.75, S 13.1; IR (KBr): $\tilde{\nu}$ = 3300, 3417 (ν_{NH_2}), 1606 cm^{-1} ($\nu_{C=S}$).

The phase purity of bulk samples of complexes **1**–**3** was confirmed by powder X-ray diffraction. The experimental data were in good agreement with simulated data (see Figure S12 of the Supporting Information).

Synthesis of $[Zn(L)_2Cl_2]$ (1-Zn)

A similar synthetic procedure was followed as for **1**, except that $ZnCl_2$ (0.895 g, 6.57 mmol) was used in place of $CoCl_2{\cdot}6H_2O$. Yield: 0.9 g (42.4%). Elemental analysis calcd (%): C 8.33, H 2.79, N 19.42, S 22.23; found: C 8.5, H 2.6, N 19.3, S 22.4; IR (KBr): $\tilde{\nu}$ = 3312, 3386 cm^{-1} (ν_{NH_2}), 1591 cm^{-1} ($\nu_{C=S}$).

Synthesis of $[Zn(L)_2Br_2]$ (2-Zn)

A similar synthetic procedure was followed as for **2**, except that $ZnBr_2$ (1.48 g, 6.57 mmol) was used in place of $CoBr_2$. Yield 0.59 g (34.7%). Elemental analysis calcd (%): C 6.36, H 2.14, N 14.7, S 17.2; found: C 6.3, H 2.22, N 14.7, S 17.2; IR (KBr): $\tilde{\nu}$ = 3342, 3401 (ν_{NH_2}), 1618 cm^{-1} ($\nu_{C=S}$).

Synthesis of $[Zn(L)_2I_2]$ (3-Zn)

A similar synthetic procedure was followed as for **3**, except that ZnI_2 (2.1 g, 6.57 mmol) was used in place of CoI_2. Yield: 0.62 g (41%). Elemental analysis calcd (%): C 5.10, H 1.71, N 11.88, S 13.6; found: C 5.17, H 1.65, N 11.96, S 13.42; IR (KBr): $\tilde{\nu}$ = 3285, 3362 (ν_{NH_2}), 1584 cm^{-1} ($\nu_{C=S}$).

The unit cells were determined for single crystals of **1-Zn**, **2-Zn**, and **3-Zn** and were in excellent agreement with those of the corresponding Co^{II} complexes. This implies that **1-Zn**, **2-Zn**, and **3-Zn** have similar packing diagrams to **1**, **2**, and **3**, respectively. To obtain further concrete evidence, we recorded powder X-ray diffraction patterns for **1-Zn**, **2-Zn**, and **3-Zn**, which were in excellent agreement with the simulated data derived from single-crystal data for their Co^{II} analogues (see Figure S13 of the Supporting Information).

Preparation of 10% diluted sample of 1

Solid $CoCl_2{\cdot}6H_2O$ (0.156 g, 0.657 mmol) and $ZnCl_2$ (0.807 g, 5.92 mmol) were added to ethanol at 35–40 °C. To this solution L (1 g, 13.2 mmol) was added and the reaction mixture was heated under reflux for 12 h. The ethanol solvent was removed under reduced pressure (rotovap) after cooling the reaction mixture. The product was extracted with acetonitrile. Needle-shaped, light blue single crystals were grown by diffusion of diethyl ether into the acetonitrile solution for one week at room temperature.

Preparation of 10% diluted sample of 2

Solid $CoBr_2$ (0.144 g, 0.657 mmol) and $ZnBr_2$ (0.666 g, 5.92 mmol) were added ethanol at 35–40 °C. To this solution L (1 g, 13.2 mmol) was added and the reaction mixture was heated under reflux for 12 h. The product was extracted with ethyl acetate. Light blue single crystals were obtained by slow evaporation of the ethyl acetate solution.

Preparation of 10% diluted sample of 3

Solid CoI_2 (0.206 g, 0.657 mmol) and ZnI_2 (1.88 g, 5.92 mmol) were added to ethanol at 35–40 °C. To this solution L (1 g, 13.2 mmol)

was added and the reaction mixture was heated under reflux for 12 h. The product was extracted with ethyl acetate. Light green single crystals were obtained by slow evaporation of the ethyl acetate solution.

CCDC 1504900 (**1**), 1504901 (**2**), and 1504902 (**3**) contain the supplementary crystallographic data for this paper. These data are provided free of charge by The Cambridge Crystallographic Data Centre.

Acknowledgements

M.S. thanks the funding agencies DST, DST Nanomission, INSA, and IIT Bombay for financial support. S.V. and P.S. thanks CSIR for financial support. K.A. thanks UGC for financial support. G.R. would like to thank SERB-DST, INSA for funding (EMR/2014/000247).

Conflict of interest

The authors declare no conflict of interest.

Keywords: ab initio calculations · cobalt · halides · magnetic properties · S ligands

[1] a) R. Sessoli, D. Gatteschi, A. Caneschi, M. A. Novak, *Nature* **1993**, *365*, 141 – 143; b) A. Caneschi, D. Gatteschi, R. Sessoli, A. L. Barra, L. C. Brunel, M. Guillot, *J. Am. Chem. Soc.* **1991**, *113*, 5873 – 5874.

[2] a) A. Nava, L. Rigamonti, E. Zangrando, R. Sessoli, W. Wernsdorfer, A. Cornia, *Angew. Chem. Int. Ed.* **2015**, *54*, 8777 – 8782; *Angew. Chem.* **2015**, *127*, 8901 – 8906; b) A. M. Ako, V. Mereacre, Y. Lan, W. Wernsdorfer, R. Clerac, C. E. Anson, A. K. Powell, *Inorg. Chem.* **2010**, *49*, 1 – 3; c) R. Pattacini, P. Teo, J. Zhang, Y. Lan, A. K. Powell, J. Nehrkorn, O. Waldmann, T. S. A. Hor, P. Braunstein, *Dalton Trans.* **2011**, *40*, 10526 – 10534; d) M. Ibrahim, Y. Lan, B. S. Bassil, Y. Xiang, A. Suchopar, A. K. Powell, U. Kortz, *Angew. Chem. Int. Ed.* **2011**, *50*, 4708 – 4711; *Angew. Chem.* **2011**, *123*, 4805 – 4808; e) Y.-Z. Zhang, A. J. Brown, Y.-S. Meng, H.-L. Sun, S. Gao, *Dalton Trans.* **2015**, *44*, 2865 – 2870; f) Y.-Y. Zhu, C. Cui, K. Qian, J. Yin, B.-W. Wang, Z.-M. Wang, S. Gao, *Dalton Trans.* **2014**, *43*, 11897 – 11907; g) C.-L. Zhou, Z.-M. Wang, B.-W. Wang, S. Gao, *Polyhedron* **2011**, *30*, 3279 – 3283; h) Y.-Y. Zhu, X. Guo, C. Cui, B.-W. Wang, Z.-M. Wang, S. Gao, *Chem. Commun.* **2011**, *47*, 8049 – 8051; i) A. Perivolaris, A. M. Fidelli, R. Inglis, V. G. Kessler, A. M. Z. Slawin, E. K. Brechin, G. S. Papaefstathiou, *J. Coord. Chem.* **2014**, *67*, 3972 – 3986; j) S. M. Taylor, J. M. Frost, R. McLellan, R. D. McIntosh, E. K. Brechin, S. J. Dalgarno, *CrystEngComm* **2014**, *16*, 8098 – 8101; k) J. Martinez-Lillo, N. Dolan, E. K. Brechin, *Dalton Trans.* **2013**, *42*, 12824 – 12827; l) Y.-Z. Zhang, S. Gomez-Coca, A. J. Brown, M. R. Saber, X. Zhang, K. R. Dunbar, *Chem. Sci.* **2016**, *7*, 6519 – 6527; m) S. K. Langley, R. A. Stott, N. F. Chilton, B. Moubaraki, K. S. Murray, *Chem. Commun.* **2011**, *47*, 6281 – 6283; n) S.-S. Bao, L.-M. Zheng, *Coord. Chem. Rev.* **2016**, *319*, 63 – 85; o) T. K. Prasad, G. Poneti, L. Sorace, M. J. Rodriguez-Douton, A.-L. Barra, P. Neugebauer, L. Costantino, R. Sessoli, A. Cornia, *Dalton Trans.* **2012**, *41*, 8368 – 8378; p) M. Murrie, *Chem. Soc. Rev.* **2010**, *39*, 1986 – 1995; q) Y.-Y. Zhu, Y.-Q. Zhang, T.-T. Yin, C. Gao, B.-W. Wang, S. Gao, *Inorg. Chem.* **2015**, *54*, 5475 – 5486.

[3] A. M. Ako, I. J. Hewitt, V. Mereacre, R. Clerac, W. Wernsdorfer, C. E. Anson, A. K. Powell, *Angew. Chem. Int. Ed.* **2006**, *45*, 4926 – 4929; *Angew. Chem.* **2006**, *118*, 5048 – 5051.

[4] C. J. Milios, R. Inglis, A. Vinslava, R. Bagai, W. Wernsdorfer, S. Parsons, S. P. Perlepes, G. Christou, E. K. Brechin, *J. Am. Chem. Soc.* **2007**, *129*, 12505 – 12511.

[5] a) M. N. Leuenberger, D. Loss, *Nature* **2001**, *410*, 789 – 793; b) J. Lehmann, A. Gaita-Arino, E. Coronado, D. Loss, *Nat. Nanotechnol.* **2007**, *2*, 312 – 317; c) L. Bogani, W. Wernsdorfer, *Nat. Mater.* **2008**, *7*, 179 – 186; d) R. Sessoli, M.-E. Boulon, A. Caneschi, M. Mannini, L. Poggini, F. Wilhelm, A. Rogalev, *Nat. Phys.* **2015**, *11*, 69 – 74.

[6] F. Neese, D. A. Pantazis, *Faraday Discuss.* **2011**, *148*, 229 – 238.

[7] a) D. E. Freedman, W. H. Harman, T. D. Harris, G. J. Long, C. J. Chang, J. R. Long, *J. Am. Chem. Soc.* **2010**, *132*, 1224 – 1225; b) R. Ruamps, R. Maurice, L. Batchelor, M. Boggio-Pasqua, R. Guillot, A. L. Barra, J. Liu, E.-E. Bendeif, S. Pillet, S. Hill, T. Mallah, N. Guihery, *J. Am. Chem. Soc.* **2013**, *135*, 3017 – 3026; c) S. Gomez-Coca, D. Aravena, R. Morales, E. Ruiz, *Coord. Chem. Rev.* **2015**, *289 – 290*, 379 – 392; d) A. K. Bar, C. Pichon, J.-P. Sutter, *Coord. Chem. Rev.* **2016**, *308*, 346 – 380; e) G. A. Craig, M. Murrie, *Chem. Soc. Rev.* **2015**, *44*, 2135 – 2147; f) J. M. Zadrozny, M. Atanasov, A. M. Bryan, C.-Y. Lin, B. D. Rekken, P. P. Power, F. Neese, J. R. Long, *Chem. Sci.* **2013**, *4*, 125 – 138; g) R. C. Poulten, M. J. Page, A. G. Algarra, J. J. Le Roy, I. Lopez, E. Carter, A. Llobet, S. A. Macgregor, M. F. Mahon, D. M. Murphy, M. Murugesu, M. K. Whittlesey, *J. Am. Chem. Soc.* **2013**, *135*, 13640 – 13643; h) P. P. Samuel, K. C. Mondal, N. Amin Sk, H. W. Roesky, E. Carl, R. Neufeld, D. Stalke, S. Demeshko, F. Meyer, L. Ungur, L. F. Chibotaru, J. Christian, V. Ramachandran, J. van Tol, N. S. Dalal, *J. Am. Chem. Soc.* **2014**, *136*, 11964 – 11971; i) C. G. Werncke, E. Suturina, P. C. Bunting, L. Vendier, J. R. Long, M. Atanasov, F. Neese, S. Sabo-Etienne, S. Bontemps, *Chem. Eur. J.* **2016**, *22*, 1668 – 1674; j) Y.-S. Meng, Z. Mo, B.-W. Wang, Y.-Q. Zhang, L. Deng, S. Gao, *Chem. Sci.* **2015**, *6*, 7156 – 7162.

[8] a) J. M. Zadrozny, D. J. Xiao, M. Atanasov, G. J. Long, F. Grandjean, F. Neese, J. R. Long, *Nat. Chem.* **2013**, *5*, 577 – 581; b) X.-N. Yao, J.-Z. Du, Y.-Q. Zhang, X.-B. Leng, M.-W. Yang, S.-D. Jiang, Z.-X. Wang, Z.-W. Ouyang, L. Deng, B.-W. Wang, S. Gao, *J. Am. Chem. Soc.* **2017**, *139*, 373 – 380.

[9] a) C. Rajnak, J. Titis, I. Salitros, R. Boca, O. Fuhr, M. Ruben, *Polyhedron* **2013**, *65*, 122 – 128; b) D. Wu, X. Zhang, P. Huang, W. Huang, M. Ruan, Z. W. Ouyang, *Inorg. Chem.* **2013**, *52*, 10976 – 10982.

[10] a) F. Habib, O. R. Luca, V. Vieru, M. Shiddiq, I. Korobkov, S. I. Gorelsky, M. K. Takase, L. F. Chibotaru, S. Hill, R. H. Crabtree, M. Murugesu, *Angew. Chem. Int. Ed.* **2013**, *52*, 11290 – 11293; *Angew. Chem.* **2013**, *125*, 11500 – 11503; b) T. Jurca, A. Farghal, P.-H. Lin, I. Korobkov, M. Murugesu, D. S. Richeson, *J. Am. Chem. Soc.* **2011**, *133*, 15814 – 15817; c) D. Schweinfurth, M. G. Sommer, M. Atanasov, S. Demeshko, S. Hohloch, F. Meyer, F. Neese, B. Sarkar, *J. Am. Chem. Soc.* **2015**, *137*, 1993 – 2005; d) R. Ruamps, L. J. Batchelor, R. Guillot, G. Zakhia, A.-L. Barra, W. Wernsdorfer, N. Guihery, T. Mallah, *Chem. Sci.* **2014**, *5*, 3418 – 3424; e) T. J. Woods, M. F. Ballesteros-Rivas, S. Gomez-Coca, E. Ruiz, K. R. Dunbar, *J. Am. Chem. Soc.* **2016**, *138*, 16407 – 16416.

[11] a) F. Yang, Q. Zhou, Y. Zhang, G. Zeng, G. Li, Z. Shi, B. Wang, S. Feng, *Chem. Commun.* **2013**, *49*, 5289 – 5291; b) M. Idesicova, J. Titis, J. Krzystek, R. Boca, *Inorg. Chem.* **2013**, *52*, 9409 – 9417; c) L. Smolko, J. Cernak, M. Dusek, J. Titis, R. Boca, *New J. Chem.* **2016**, *40*, 6593 – 6598; d) L. Smolko, J. Cernak, J. Kuchar, R. Boca, *Monatsh. Chem.* **2015**, *146*, 243 – 248; e) F. Habib, I. Korobkov, M. Murugesu, *Dalton Trans.* **2015**, *44*, 6368 – 6373; f) E. Colacio, J. Ruiz, E. Ruiz, E. Cremades, J. Krzystek, S. Carretta, J. Cano, T. Guidi, W. Wernsdorfer, E. K. Brechin, *Angew. Chem. Int. Ed.* **2013**, *52*, 9130 – 9134; *Angew. Chem.* **2013**, *125*, 9300 – 9304; g) Y.-Y. Zhu, C. Cui, Y.-Q. Zhang, J.-H. Jia, X. Guo, C. Gao, K. Qian, S.-D. Jiang, B.-W. Wang, Z.-M. Wang, S. Gao, *Chem. Sci.* **2013**, *4*, 1802 – 1806; h) S. Sottini, G. Poneti, S. Ciattini, N. Levesanos, E. Ferentinos, J. Krzystek, L. Sorace, P. Kyritsis, *Inorg. Chem.* **2016**, *55*, 9537 – 9548; i) S. Ziegenbalg, D. Hornig, H. Goerls, W. Plass, *Inorg. Chem.* **2016**, *55*, 4047 – 4058.

[12] a) E. A. Suturina, D. Maganas, E. Bill, M. Atanasov, F. Neese, *Inorg. Chem.* **2015**, *54*, 9948 – 9961; b) D. Maganas, S. Sottini, P. Kyritsis, E. J. J. Groenen, F. Neese, *Inorg. Chem.* **2011**, *50*, 8741 – 8754; c) S. Vaidya, S. Tewary, S. K. Singh, S. K. Langley, K. S. Murray, Y. Lan, W. Wernsdorfer, G. Rajaraman, M. Shanmugam, *Inorg. Chem.* **2016**, *55*, 9564 – 9578.

[13] a) S. Vaidya, A. Upadhyay, S. K. Singh, T. Gupta, S. Tewary, S. K. Langley, J. P. S. Walsh, K. S. Murray, G. Rajaraman, M. Shanmugam, *Chem. Commun.* **2015**, *51*, 3739 – 3742; b) J. M. Zadrozny, J. Telser, J. R. Long, *Polyhedron* **2013**, *64*, 209 – 217.

[14] J. M. Zadrozny, J. R. Long, *J. Am. Chem. Soc.* **2011**, *133*, 20732 – 20734.

[15] N. F. Chilton, R. P. Anderson, L. D. Turner, A. Soncini, K. S. Murray, *J. Comput. Chem.* **2013**, *34*, 1164 – 1175.

[16] a) M. Dey, S. Dutta, B. Sarma, R. C. Deka, N. Gogoi, *Chem. Commun.* **2016**, *52*, 753 – 756; b) A. Eichhoefer, Y. Lan, V. Mereacre, T. Bodenstein, F. Weigend, *Inorg. Chem.* **2014**, *53*, 1962 – 1974; c) D. V. Korchagin, G. V.

Shilov, S. M. Aldoshin, R. B. Morgunov, A. D. Talantsev, E. A. Yureva, *Polyhedron* **2015**, *102*, 147 – 151.

[17] a) V. V. Novikov, A. A. Pavlov, A. S. Belov, A. V. Vologzhanina, A. Savitsky, Y. Z. Voloshin, *J. Phys. Chem. Lett.* **2014**, *5*, 3799 – 3803; b) J. Pilbrow, *Transition Ion Electron Paramagnetic Resonance*, Clarendon, Oxford, **1990**.

[18] a) J. M. Zadrozny, J. Liu, N. A. Piro, C. J. Chang, S. Hill, J. R. Long, *Chem. Commun.* **2012**, *48*, 3927 – 3929; b) S. Gomez-Coca, E. Cremades, N. Aliaga-Alcalde, E. Ruiz, *J. Am. Chem. Soc.* **2013**, *135*, 7010 – 7018; c) W. Huang, T. Liu, D. Wu, J. Cheng, Z. W. Ouyang, C. Duan, *Dalton Trans.* **2013**, *42*, 15326 – 15331.

[19] S. Gomez-Coca, A. Urtizberea, E. Cremades, P. J. Alonso, A. Camon, E. Ruiz, F. Luis, *Nat. Commun.* **2014**, *5*, 4300.

[20] E. A. Suturina, J. Nehrkorn, J. M. Zadrozny, J. Liu, M. Atanasov, T. Weyhermueller, D. Maganas, S. Hill, A. Schnegg, E. Bill, J. R. Long, F. Neese, *Inorg. Chem.* **2017**, *56*, 3102 – 3118.

[21] a) D. Ganyushin, F. Neese, *J. Chem. Phys.* **2006**, *125*, 024103; b) F. Neese, T. Petrenko, D. Ganyushin, G. Olbrich, *Coord. Chem. Rev.* **2007**, *251*, 288 – 327.

[22] S. Ye, F. Neese, *J. Chem. Theory Comput.* **2012**, *8*, 2344 – 2351.

[23] *Computational Organometallic Chemistry* (Ed.: T. Cundari) Marcel Dekker, New York, **2001**.

[24] R. Maurice, R. Bastardis, C. de Graaf, N. Suaud, T. Mallah, N. Guihery, *J. Chem. Theory Comput.* **2009**, *5*, 2977 – 2984.

[25] S. K. Singh, J. Eng, M. Atanasov, F. Neese, *Coord. Chem. Rev.* **2017**, *344*, 2 – 25.

[26] Y. Rechkemmer, F. D. Breitgoff, M. van der Meer, M. Atanasov, M. Hakl, M. Orlita, P. Neugebauer, F. Neese, B. Sarkar, J. van Slageren, *Nat. Commun.* **2016**, *7*, 10467.

[27] J. Vallejo, I. Castro, R. Ruiz-Garcia, J. Cano, M. Julve, F. Lloret, G. De Munno, W. Wernsdorfer, E. Pardo, *J. Am. Chem. Soc.* **2012**, *134*, 15704 – 15707.

[28] a) V. V. Novikov, A. A. Pavlov, Y. V. Nelyubina, M.-E. Boulon, O. A. Varzatskii, Y. Z. Voloshin, R. E. P. Winpenny, *J. Am. Chem. Soc.* **2015**, *137*, 9792 – 9795; b) L. Smolko, J. Cernak, M. Dusek, J. Miklovic, J. Titis, R. Boca, *Dalton Trans.* **2015**, *44*, 17565 – 17571.

[29] F. Neese, *Wiley Interdiscip. Rev. Comput. Mol. Sci.* **2012**, *2*, 73 – 78.

[30] a) C. Angeli, R. Cimiraglia, S. Evangelisti, T. Leininger, J. P. Malrieu, *J. Chem. Phys.* **2001**, *114*, 10252 – 10264; b) C. Angeli, R. Cimiraglia, J.-P. Malrieu, *Chem. Phys. Lett.* **2001**, *350*, 297 – 305.

[31] B. A. Hess, *Phys. Rev. A* **1986**, *33*, 3742 – 3748.

[32] F. Neese, *J. Comput. Chem.* **2003**, *24*, 1740 – 1747.

Manuscript received: December 27, 2016
Accepted manuscript online: May 17, 2017
Version of record online: June 29, 2017